The Use of 3D Magnetotellurics in Mineral Exploration: Synthetic Model Study and Inversion of 3D MT Survey Data from the Wirrda Well IOCG (SA, Australia)

Thesis submitted in accordance with the requirements of the University of Adelaide for an Honours Degree in Geophysics

James David Komenza

November 2013

THE UNIVERSITY of ADELAIDE

ABSTRACT

As a consequence of diminishing shallow mineral resources, the exploration industry has turned its focus to deeper targets. For this reason, the magnetotelluric (MT) method has gained much attention due to its unique penetration in regions of thick cover sequences. As the setting and geometries of mineral deposits are often complex, three-dimensional (3D) models are required for their interpretation. Though still computationally demanding, 3D inversion is now becoming a practical and common tool for presenting MT data. However, there has been little critical analysis of the ability of 3D MT surveys to recover structural geometry. To assess the value of 3D MT in the exploration of mineral deposits, this study compares results of synthetic model studies with a 3D MT survey from an iron oxide copper gold (IOCG) deposit in South Australia. Synthetic data sets are presented for two scenarios incorporating a conductive 3D target, with and without conductive cover. A comparison of model responses demonstrate that while MT is greatly sensitive to conductive and symmetrical bodies at depth, its resolution for detecting finite 3D bodies is significantly reduced under conductive cover. Although 2D inversions can recover the geometry of finite conductive bodies, it is possible to successfully interpret 2D survey data using 3D inversion algorithms. Utilising all components of the impedance tensor, off-profile 3D conductive structure can be obtained from 2D survey data alone. Results of the synthetic studies were applied to a 3D MT data set acquired across the Wirrda Well IOCG deposit (SA, South Australia). Although the thickness of conductive cover sequences were resolved from 2D and 3D inversion, conductivity structure associated with alteration and mineralisation could not be recovered. Thus, although 3D MT shows promise for recovering 3D conductivity structures at depth, its use in delineating deposit scale targets under conductive cover is greatly limited.

KEYWORDS

Magnetotellurics, mineral exploration, two dimensional inversion, three-dimensional inversion, synthetic model studies, Wirrda Well, IOCG

TABLE OF CONTENTS

LIST OF FIGURES

LIST OF TABLES

INTRODUCTION

As a consequence of diminishing shallow and easily detectable resources, the exploration industry has turned its focus to deeper ore bodies with little success (Schodde 2010, Ferguson 2012). Subsequently, initiatives such as the Deep Exploration Technologies Cooperative Research Centre (DET CRC), and the Australian Academy of Science's UNCOVER proposal have been developed to address these problems. Such programs have been founded upon the realisation that majority of Australia's future discoveries will demonstrate little to no surface expression, and are potentially buried under large amounts of cover.

Ore deposits occur at the location of large energy and mass flux systems, often associated with intrusive activity. During ore genesis, large volumes of rock can be fractured, hydrothermally altered, and mineralised (Lowell & Guilbert 1970, Guilbert & Lowell 1974, Sillitoe 2010). As hydrothermally altered minerals and ore-hosting rocks are associated with anomalous electrical properties (Kearey 2002), changes in conductivity will exist between unaltered host rock and mineralised systems. Additionally, the geological structure and setting of deposits is often complex, and regularly requires three dimensional (3D) models for interpretation.

In the last decade, the magnetotelluric (MT) method has attracted much interest stemming from its enormous depth range, sensitivity to conductors, and vast improvements in instrumentation and processing (Varentsov *et al.* 2013). Although MT cannot recover compact and conductive bodies at depth, a paradigm is that 3D MT

surveys may resolve the structural geometries of large style mineral deposits and alteration zones under cover.

With recent advances in computation, modelling, and inversion, 3D MT surveys are becoming increasingly common. A number of 3D inversion codes have now been written (Mackie *et al.* 1994, Newman & Alumbaugh 2000, Sasaki 2004, Siripunvaraporn *et al.* 2005a), and many model studies have been published demonstrating their proficiencies (e.g. Siripunvaraporn *et al.* 2005b, Han *et al.* 2009, Miensopust *et al.* 2013). However, only a few practical examples for mineral exploration have been presented (e.g. Farquharson & Craven 2009, Li *et al.* 2011, Chen *et al.* 2012), and very few synthetic model studies have been published (Morrison & Nichols 1997, Tuncer *et al.* 2006). Subsequently, there has been little critical analysis of what can, or cannot be recovered from two dimensional (2D) and 3D inversion of MT data above mineral deposits.

In this study, two 3D numerical models have been developed for an idealised target anomaly, with and without conductive overburden. Forward calculations of surface MT responses have been executed for the given models, including a 3D grid and 2D profile. Apparent resistivity and phase curves are presented for both scenarios, as well as impedance phase tensors (Caldwell *et al.* 2004) and Parkinson induction arrows (Parkinson 1959, Lilley & Arora 1982) for all model sites. The RLM2DI (Rodi & Mackie 2001) and WSINV3DMT (Siripunvaraporn *et al.* 2005a) algorithms have been applied to each data set to determine the detectability of the target anomaly and recover its simple geometry. In the final component of this thesis, the results of the synthetic

model study have been applied to a real 3D MT data set from the Wirrda Well Iron Oxide Copper Gold deposit (Vella 1997), 20 km south of Olympic Dam (SA, South Australia).

THE MAGNETOTELLURIC METHOD

Magnetotellurics is a passive electromagnetic method that measures variations of Earth's electric field, **E**, and magnetic induction, **B**, at the surface over time to determine conductive structure at depth. In the frequency domain, the relationship between the orthogonal components of **E** and **B** is defined by the impedance tensor, $\underline{\underline{\boldsymbol{Z}}}$**:**

$$\begin{pmatrix} E_x \\ E_x \end{pmatrix} = \begin{pmatrix} Z_{xx} & Z_{xy} \\ Z_{yx} & Z_{yy} \end{pmatrix} \begin{pmatrix} B_x/\mu_0 \\ B_y/\mu_0 \end{pmatrix} \; or \; \boldsymbol{E} = \underline{\underline{Z}}\boldsymbol{B}/\mu_0 \, , \qquad (-1-)$$

where for studies of the Earth, μ_0 is assigned the free-space value of $4\pi \bullet 10^{-7}$ and x and y are the orthogonal orientations, typically in the north and east directions. As $\underline{\underline{Z}}$ is complex valued, it is composed of both real and imaginary parts (which can be expressed as an in-phase and out of phase component). Thus, each component of $\underline{\underline{\mathbf{Z}}}$, $\mathbf{Z_{ij}}$, has not only a magnitude, but also an impedance phase angle (ϕ) resulting from the lag and attenuation of electromagnetic waves as they penetrate Earth (Simpson & Bahr 2005) :

$$\phi_{ij} = tan^{-1}\left(\frac{Im\{Z_{ij}\}}{Re\{Z_{ij}\}}\right) \qquad (-2-)$$

Magnetotelluric impedance information is generally presented in terms of an apparent resistivity (ρ_a), defined as the average resistivity of an equivalent uniform half-space for any given sounding period (Simpson & Bahr 2005):

$$\rho_{a,ij(\omega)} = \frac{1}{\mu_0 \omega} \left| Z_{ij}(\omega) \right|^2, \quad \text{(-3-)}$$

where ρ_a is given in ohm metres (Ωm), ω is the angular frequency in radians per second (s^{-1}) and Z_{ij} is in ohms (Ω).

For 2D geoelectrical structures, the electromagnetic fields can be decoupled into two independent modes: the Transverse Electric (TE) and Transverse Magnetic (TM) mode. The TE mode incorporates electric fields parallel to geoelectric strike (E_x), with induced magnetic fields perpendicular to strike (B_y) and in the vertical plane (B_z). The TM mode incorporates magnetic fields parallel to strike (H_x), with induced electric fields perpendicular to strike (E_y) and in the vertical plane (E_z) (Simpson & Bahr 2005). In this study, electric fields are described as being linearly polarised parallel (**x**) and perpendicular (**y**) to the local geoelectric strike orientation, and are annotated as TE and TM respectively.

Fundamental to exploration MT is the realisation that electromagnetic responses from increasing depths can be retrieved with increasing MT sounding periodicity (Tikhonov 1950, Cagniard 1953). Electromagnetic fields naturally induced in Earth have periodicities ranging between 10^{-4} s to 10^5 s. However, electromagnetic induction is governed by diffusion and the skin effect (Simpson & Bahr 2005) resulting in period-dependent penetration depths. The electromagnetic skin depth equation describes this phenomenon, resulting from the exponential decay of electromagnetic fields as they diffuse into Earth:

$$\delta(T) \approx 500 \sqrt{T \rho_a}, \quad \text{(-4-)}$$

where δ (T) is the skin depth in meters at period T (seconds) (Simpson & Bahr 2005). Thus, for any MT sounding period, the penetration depth is also dependent on the average resistivity structure of the volume of earth that it penetrates. For one skin depth, electromagnetic fields are attenuated to e^{-1} (~37%) of their amplitudes at the surface, and are considered insensitive to conductors below this depth. Subsequently, longer sounding periods are required to detect targets deep and under conductive structure, albeit at increasingly less resolution.

Geomagnetic Depth Sounding (GDS) and Parkinson Induction Arrows

The vertical magnetic field, B_z, can also be measured to utilize a technique known as Geomagnetic Depth Sounding (GDS). The GDS approach is based on measuring three components of the magnetic field (B_x, B_y, B_z), where perturbations in B_z are caused only by the interaction of the horizontal magnetic field and lateral conductivity changes in Earth (Simpson & Bahr 2005). B_z is related to the horizontal magnetic fields through the complex valued tensor **T:**

$$[B_z] = [T_{zx} \quad T_{zy}] \begin{bmatrix} B_x \\ B_y \end{bmatrix} \qquad (5)$$

Induction arrows are commonly used to present GDS data, and are based on both the real and imaginary components of **T**. Following the Parkinson convention, the real part of the induction arrow points towards conductors, and away from resistors (Parkinson 1959, Lilley & Arora 1982). Also, as **T** is period dependent, induction arrows can be made for a range of periods, demonstrating the change in lateral resistivity structure with depth (Equation 4).

Phase Tensors

The phase tensor is a graphical representation of the impedance tensor, insensitive to near-surface distortion (Caldwell *et al.* 2004). Phase tensors demonstrate the horizontal direction of maximum and minimum induction current through the use of an ellipse (Bibby *et al.* 2005). The ellipticity (λ) of the phase tensor is defined as:

$$\lambda = \frac{|\phi_{max} - \phi_{min}|}{\phi_{max} - \phi_{min}}, \quad (6)$$

where ϕ_{max} and ϕ_{min} are the maximum and minimum axes of the ellipse, and equal values indicate 1D geoelectric structure. The maximum induction direction is represented by ϕ_{max}, which indicates the direction of lowest resistivity. The degree of ellipticity and size of the phase tensor indicates the strength of the orientation dependent induction currents. Phase tensors are typically presented with colour fills corresponding to one of the principal components (ϕ_{max} or ϕ_{min}), or skew angle (β_0). The skew angle is a measure of 3D symmetry, where high skew values ($|\beta_0| > 5$) often indicate three dimensional structure (Booker 2013). The skew angle is equal to the difference between the direction of highest conductivity and geoelectric strike (Bibby *et al.* 2005).

SYNTHETIC MODEL STUDY

Two conceptual 3D resistivity models were developed to investigate the sensitivity of MT to delineate sub-surface structure, with and without conductive cover. Forward calculations were executed for each numerical scenario. The resulting synthetic data is presented as apparent resistivity and phase responses, as well as map view phase tensor and induction arrow plots. 2D and 3D inversion algorithms have been applied to this data, and representative model results are presented.

Model Design and Forward Calculations

Each synthetic model was based on a simple 3D design, comprised of a 3D conductive target anomaly within a resistive basement. **Model A** incorporates a conductive 1 Ωm 2 km x 2 km x 2 km target anomaly at a depth of 550 m within a 1000 Ωm basement. While **Model B** demonstrates the same model geometries, its top 250 m was designated a 10 Ωm resistivity value to replicate thick and conductive cover/regolith sequences (Figure 1a). Both scenarios represent geologically extreme conditions. However, simple and contrasting model constructions were purposely implemented so that the responses from each model could be easily understood and compared.

Forward responses were calculated in 3D for 24 periods between 10^{-4} and 10^{2} seconds (s) utilising the finite-difference code of Mackie et al. (1994). Calculations were made for 141 model sites positioned in a square grid above the target. The grid covered an area of 5 km x 5 km, with a site spacing of 500 m (see Fig 1b). Two profiles of 250 m site spacing were also created across the top of the target anomaly for densely sampled 2D and 3D profile inversions.

The forward modelling domain was a rectilinear grid (Figure 2) discretised by $N_x \bullet N_y \bullet N_z = 54 \bullet 54 \bullet 28 = 81648$ cells. Here, x, y, and z point east, north and down. The model domain extends laterally 50 km, and down 5 km. Before forward calculation, an additional 1D layered earth model was added to the bottom of each model (Table 1). For both numerical scenarios, the responses at all sites were returned by the MT forward calculation, and exported as EDI files (Wight 1988).

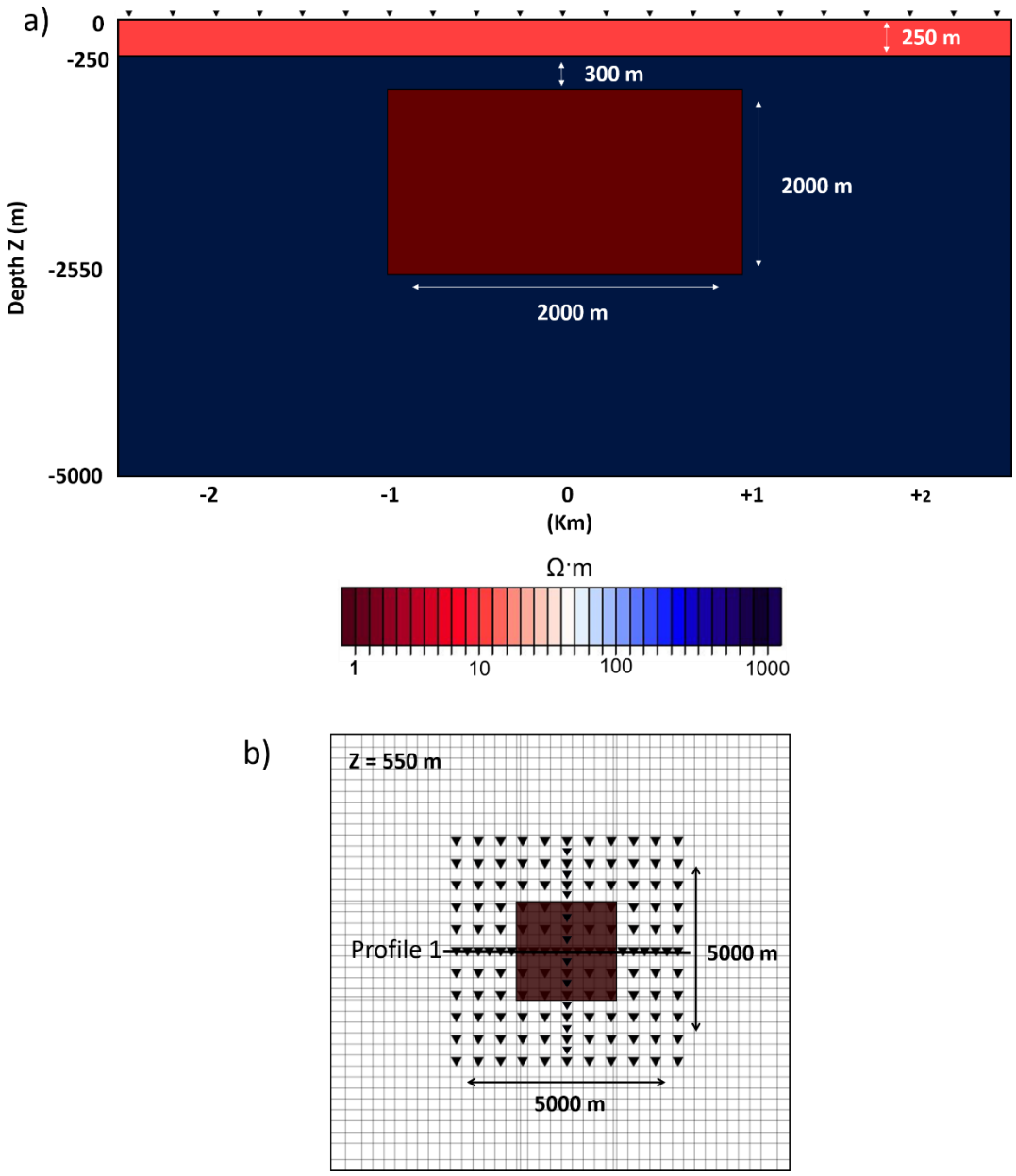

Figure 1: Forward model geometry. 1a) Vertical cross section (top) through the centre of Model B. Resistivity values and model geometries are shown, including; a conductive regolith, resistive basement, and conductive target. 1b) Horizontal slice of synthetic models A and B from 550 m to 2550 m below the survey area. The shaded triangles represent MT station sites at the surface within a 5 x 5 km grid. The lateral extent of the target anomaly is shaded for reference and Profile 1 is annotated.

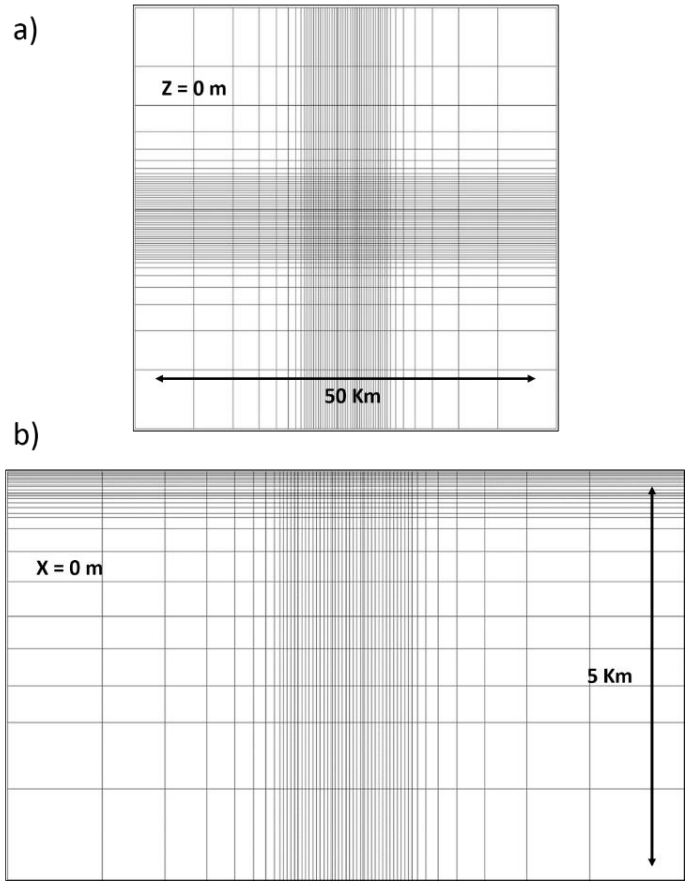

Figure 2: Rectilinear mesh used in 3D F-D modelling. 2a) Horizontal cross section (top) consisting of 54 • 54 cells corresponding to a geographical area of 50 km^2. At the core of the grid, the cell dimensions are 200 m x 200 m in size. 2b) Vertical cross section (bottom) with 28 layers extending down 5 km. Boundary conditions are imposed by a 1D base model shown in Table 1. This grid should be imagined as a cube consisting of 81648 cells.

1D Base Model

Thickness (meters)	Resistivity (Ωm)
6000	10,000
30,000	100
100,000	1000
250,000	10

Table 1. Synthetic 1D layered basal model utilised in F-D 3D modelling.

Apparent Resistivity and Phase Curves

Figure 3 shows the TE mode apparent resistivity and phase curves for each model scenario at two station locations; one (**01**) away from the target conductor, and the other (**60**) above the target conductor (see Figure 3f). As the true resistivity structures are known, penetration depths (δ) for each sounding periodicity and model scenario can be approximated from the skin depth equation (Equation 4). For **Model A**, the two response curves are divergent, indicating lateral variations in model resistivity structure. At the shortest periods of each site, impedance phases are ~ 45˚, indicating a uniform model. For site **60**, an increase in the phase of sounding periodicities > 10^{-3} seconds (δ > 500 m) is consistent with a decrease in apparent resistivity associated with the target anomaly (550 m). Conversely, site **01** demonstrates only small variations in apparent resistivity and phase between 10^{-2} s and 10^{-1} s (δ = 1600 m to 5000 m). Thus, site **01** demonstrates significantly less sensitivity to the target anomaly. The apparent resistivity values for periods longer than 10^{-2} s are approximately one order of magnitude greater at site **01** than for site **60**.

For **Model B** (250 m of regolith), response curves of site **01** and **60** fall on the same smooth curve. Impedance phases for periods smaller than 10^{-2} s (δ = 160 m) are ~ 45˚, and together with the apparent resistivity curves, indicate 1D structure within the 10 Ωm cover sequence. Periodicities that penetrate into the basement are > 0.04 s (Equation 4). Thus, the response resulting from the basement/regolith contact, and the frequencies sensitive to the target anomaly are shifted to longer sounding periodicities when compared to **Model A**. As a consequence of the conductive cover, the magnitude differences between the **Model B** site responses are small. Despite a constant shift in

apparent resistivity at periods less than 10^{-2} s, variations are within a 5% error at all 24 periods. Additionally, only 4 periods between 10^{-2} s and 10^{-1} s show phase differences greater than a corresponding 1.4˚phase error (Fig 2e).

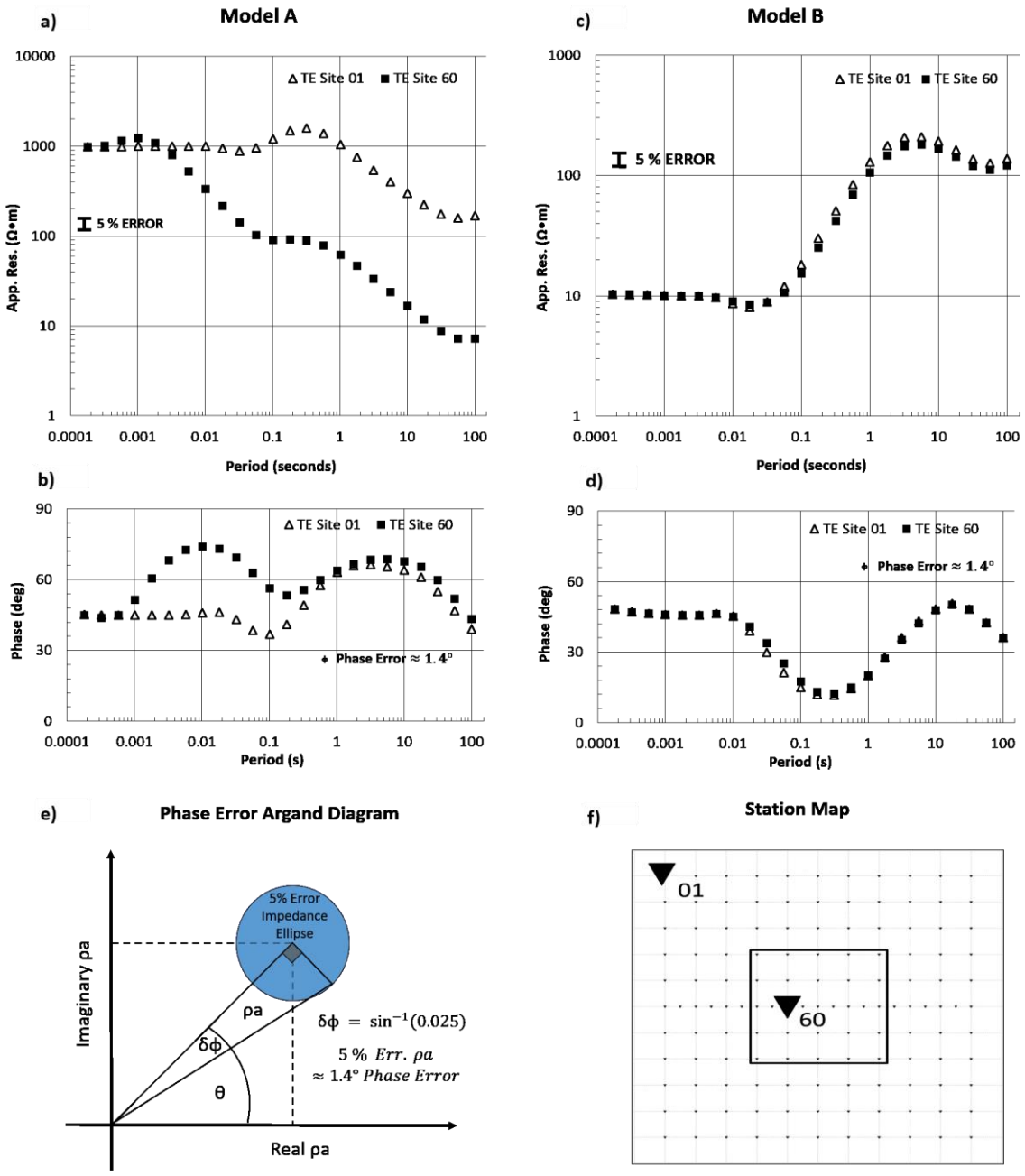

Figure 3: TE mode apparent resistivity (ρ_a) and phase (ϕ) curves of Model A and B for two station locations. 3a, b) Model A ρ_a and ϕ. 3c, d) Model B ρ_a and ϕ. For reference, a 5% error bar in ρ_a magnitude and corresponding ≈ 1.4° absolute error in phase are shown. 3e) Phase error Argand diagram demonstrating the relationship between phase and apparent resistivity standard errors. 3f) Station location map at the surface with station 01 and 60 highlighted. The lateral extent of the target anomaly is represented by a black outline.

Phase Tensor and Induction Arrows

Figure 4 shows map view phase tensor and induction arrow plots at 1 s for each synthetic model. Phase tensors have colour fills corresponding to minimum phase (ϕ_{min}) and induction arrows are plotted following the Parkinson convention, where the real component of the arrow is plotted pointing towards conductors, and away from resistors.

For **Model A**, phase angles range from 52˚to 62˚, with greatest values observed at its centre. Typically, phases > 45˚indicate a decrease in resistivity with depth, which agrees with the true model conductivity structure. The maximum axes (ϕ_{max}) of the phase tensor ellipses point towards the centre of the anomaly, indicating the direction of lowest resistivity. This is also supported by the Induction arrows, which demonstrate a rotation in geoelectric strike surrounding the anomaly. Hence, even without knowledge of the target's geometry, it is apparent that a highly conductive body exists at the centre of the survey area.

The 1 s phase tensors of **Model B** are approximately circular, indicating near 1D structure. The observed phase angles of < 20˚are indicative of the cover basement contact, where phase angles < 45˚represent an increase in resistivity with depth. All induction arrows point towards the target anomaly. However, their magnitudes are less than 0.01, which is less than typical noise in real data.

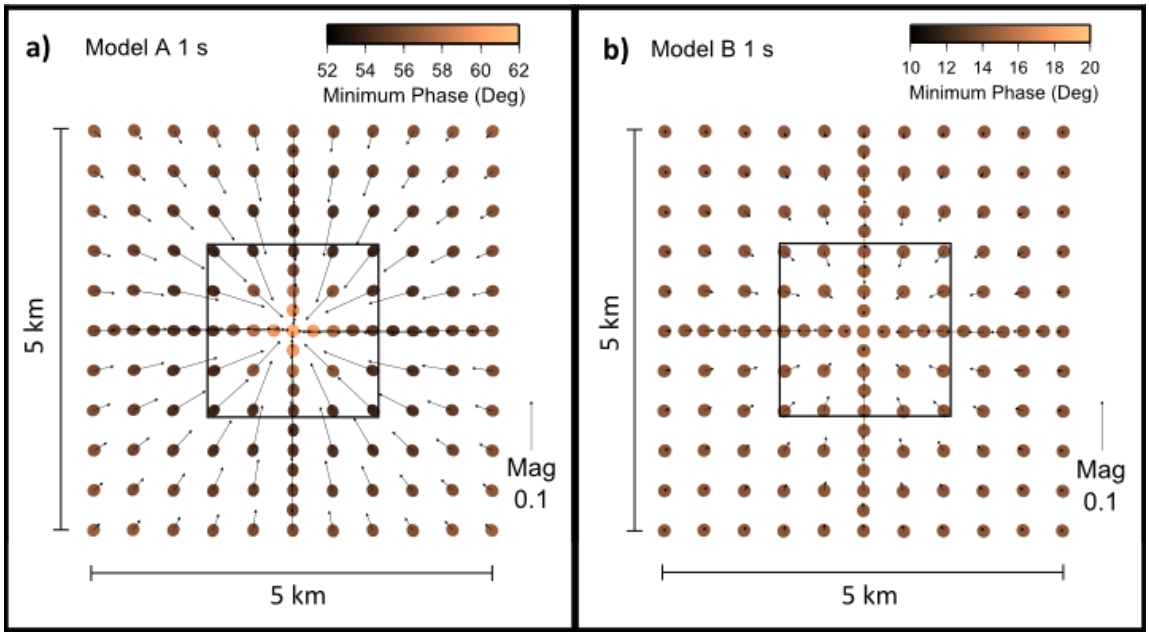

Figure 4: Map view phase tensor and real component Parkinson induction arrow plots for Model A and B. 4a) Model A with no cover. 4b) Model B with 250 m of 10 Ωm cover. Phase tensors: circular tensors indicate mostly 1D structure, whereas the major axes of elongate tensors indicate a strong induction polarisation. The colour of the phase tensor represents the invariant minimum phase value. Induction arrows: the real part of the induction arrow is plotted following the Parkinson convention (points towards conductor). Induction arrows point towards the centre of the target anomaly for models A and B. A normalised induction arrow with magnitude of 0.1 is shown for reference. The lateral extent of the target anomaly is indicated by a black outline.

2D MT Inversion for an Isolated 3D Body

The potential dangers of inverting 3D structure with 2D inversion algorithms are well known (Ledo *et al.* 2002, Ledo 2005, Siripunvaraporn *et al.* 2005b). In 2D inversions, only the off-diagonal components of the impedance tensor are considered (which typically means that half the impedance tensor information is not included). Despite this, successful interpretations of 3D structures with well orientated and constrained 2D inversions are possible (Ledo 2005).

2D inversions were completed for a densely sampled profile (Figure 1b) to further investigate the sensitivity of each data set to the target anomaly. Inversions were

completed utilising the RLM2DI code of Rodi and Mackie (2001) implemented by WinGlink's 2D inversion module. Changes to the settings and parameters of this code can cause significant variations in model outputs (see for instance Tietze & Ritter 2013). For this reason, inversions were completed to determine the optimal parameters for each data set, and also to test the robustness of model results. However, only representative inversion models are shown here.

2D inversions for each model scenario are shown in Figure 5. **Model A** and **B** data sets were inverted for TE and TM modes with 21 periods between 10^{-3} and 10^{2} seconds. Typical error values for good MT data range from 2 % to 8 %. Subsequently, apparent resistivity and phase errors were equally weighted, and set to 5% and 2.5% respectively. A smoothing operator, $\boldsymbol{\tau}$, controls the trade-off between fitting the data and producing smoother models. A $\boldsymbol{\tau}$ of 3 was determined to provide best model results. The inversion domain was designated a starting resistivity of 10 Ωm, and consisted of 72 rows and 123 columns. Cell sizes increased exponentially from the survey area and extended laterally 200 km, and down 150 km. Each inversion was run to convergence, returning a root mean square (RMS) misfit of 2.14 for **Model A**, and 0.17 for **Model B**.

Inversions for **Model A** (Figure 5a) demonstrate reasonable agreement with the true resistivity structure. A conductive 1 Ωm to 10 Ωm anomaly is located below the centre of the profile, extending laterally ~ 2000 m and down ~ 1000 m. Although its vertical extent was poorly resolved, the depth to the anomaly and its sides were imaged successfully.

Conversely, the inversion of **Model B** demonstrates no evidence of a subsurface conductor. The 10 Ωm cover layer is well imaged, and a sharp boundary between this unit and the basement is observed across the model. At its centre, there is a small downward flexure within the cover layer, which is consistent with the location of the buried conductor. However, without prior knowledge of the true model structure, this flexure would almost certainly be associated with a change in cover thickness.

An RMS error of less than 1 often indicates that the standard errors of the inversion are set too high. The low RMS misfit of the inversion of **Model B** (Figure 5b) is attributed to the data's insensitivity to the buried 3D structure. For this reason, inversions with error bars of 1% (ρ_a) and 0.5% (ϕ) were computed. This resulted in a much sharper model at the regolith basement contact, spurious results at depth, but no improvement in recovering the target's geometry. For real data, it would be unrealistic to expect such low errors, even with optimal equipment and operational practices.

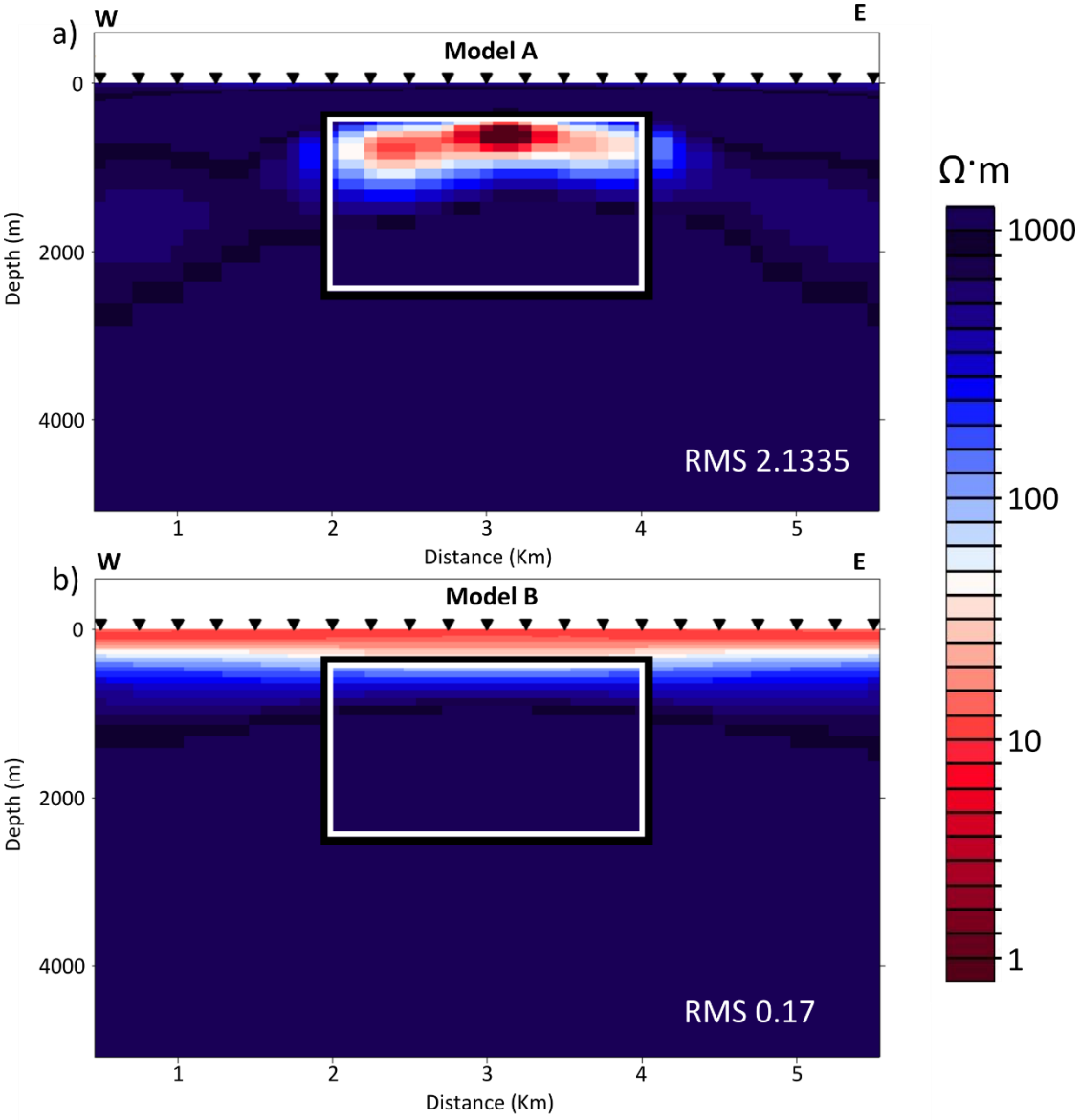

Figure 5: 2D inversion results for models A (5a) and B (5b). The profile inverted (c.f. Figure 1, Profile 1) has a site spacing of 250 m oriented west to east. The horizontal and vertical extent of the anomalous body is shown as a black outline. When no conductive overburden exists, the top and sides of the target are recovered.

2D MT Inversion for an Extended Body

As a result of overlying conductive structure, the 3D anomaly of **Model B** was not resolved. However, it is possible that exploration targets have large inductive and geological scale lengths, and can be interpreted as 2D conductivity structures at the

resolution of deposit scale surveys (e.g. Tuncer *et al.* 2006). For this reason, 3D forward calculations were repeated for a third model design with 250 m of regolith. In this scenario, the target anomaly extends horizontally throughout the entire model domain (effectively 2D). The same methods and settings were used for inverting this data as previously described, but with considerably improved results (Figure 6a). Further improvements to the model's resolution were observed after the addition of a tear at the regolith/basement contact (250 m depth). Tears in the inversion domain indicate that across a given boundary, there is an abrupt and sharp change in conductivity. Subsequently, the tear produced a distinctive separation between the regolith/basement contact and target structure. Due to this success, a tear was incorporated into additional inversions for **Model B,** to determine if resolution would be improved for the 3D case as well. RMS values of 0.76 and 0.156 were returned for inversions of the 2D and 3D target scenarios respectively, and are shown in Figure 6.

Despite a conductive regolith layer, the 2D anomaly is significantly better resolved when compared to the 3D equivalent. Although TM responses from each scenario are similar, there is a significant change in the TE responses from the extended anomalous body. This allows 2D inversion to resolve its geometry. However, as the inversion is smooth, the edges and depth extent of the anomaly are exaggerated. Despite this, the most conductive regions (~ 1 Ωm) that are resolved agree with the true model structure. Prior to the addition of a tear, the regolith layer was highly diffuse, and the relationship between both structures was unclear.

For **Model B** inversions (3D target), a reduction in RMS was observed after incorporating a tear. The regolith/basement contact was resolved, and the sensitivity of the inversion to the target improved. A region of low resistivity (~ 100 Ωm) was recovered at the approximate location of the target anomaly (Figure 6b). However, the apparent resistivity of this anomaly is one order of magnitude greater than the true model, and could easily be dismissed during interpretation. Additionally, it was unclear if this anomaly was required by the data, or was simply an inversion artefact. Numerous inversions were completed to determine the robustness of this model. Although conductive structures were repeatedly modelled below the profile, they were often smeared to great depth extents. Additionally, changes in the inversion settings and parameters sometimes lead to an inability to resolve this structure at all. Thus, although a tear at the regolith/basement contact significantly improved inversion results, this anomaly would most likely be considered an inversion artefact without prior knowledge of the true model structure.

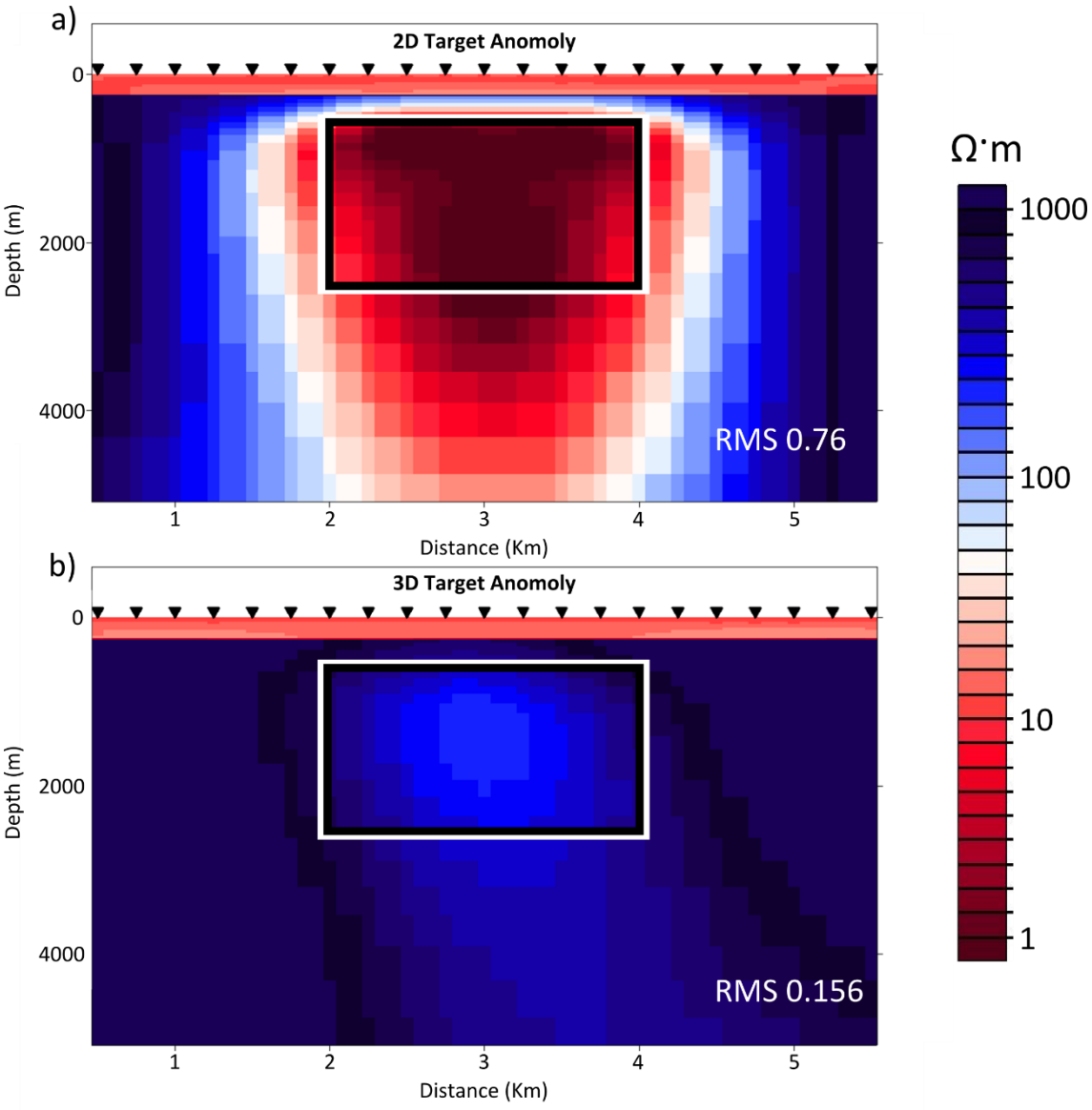

Figure 6: 2D inversions incorporating a tear at the regolith basement contact for an elongated 2D target (6a), and isolated 3D target (6b). The horizontal and vertical extent of this anomaly is shown as a black outline.

3D MT Inversion

As both **Model A** and **B** data sets contain 3D effects, it is necessary to use 3D inversions to attempt to recover the true model resistivity structures. Thus, the 3D inversion algorithm, WSINV3DMT (Siripunvaraporn *et al.* 2005a) was applied to each data set. Due to computational limitations and requirements of this code, only 59 of the

141 model stations, and 16 of the 24 periods could be inverted. Additionally, inversions utilised all complex impedance terms (8 responses, real and imaginary). The model domain was a rectilinear grid with 60 • 60 • 30 = 108000 cells in x, y and z directions. At the centre of the grid, corresponding to the centre of model stations, a uniform discretization is observed, with a cell width of ~ 200 m in x and y directions. Cell sizes increased exponentially from this location, extending laterally 80 km and down 100 km. Note that this inversion domain is not the same as F-D modelling domain (c.f. Figure 2).

The 3D inversion of **Model A** (Figure 7a) was computed from a uniform 1000 Ωm half space and a 5 % error in impedance information. 16 periods were inverted between 10^{-3} and 10^{1} s for a 500 m spaced grid with 59 stations (Figure 7d). Periodicities within this range were selected as they demonstrate the greatest sensitivity to the target anomaly, determined from the skin depth equation (Equation 4) and **Model A** TE response plots (Figure 3). The model was run with a $\boldsymbol{\tau}$ of 5, and smoothing in x, y and z directions of 0.1. An initial RMS of 10.08 decreased to 2.24 after three iterations. This result is shown in Figure 7.

The 3D inversion of **Model A** resolves a 1 Ωm to 10 Ωm conductive body below the centre of the survey area. Both the depth to the anomaly (550 m) and its width in both x and y directions (2 x 2 km) (Figure 7b) agree with the true synthetic model. However, only half of the anomalies depth extent (2 km) is resolved. Despite this, the 3D model is much sharper and demonstrates better symmetry than 2D inversion results, which is characteristic of the true geometry. The conductive regions (1 – 100 Ωm) observed outside of the survey area are interpreted as edge effects resulting from the failure to

invert for the complete data set and model grid. This is supported by the fact that the greatest edge effects are observed on the shortest sides of the survey area, where the model is less constrained by station data (Figure 7b).

Model B was inverted utilising the same station grid and errors, but for longer periods. Due to the high conductance of the regolith layer, the period-dependent penetration depth is reduced (Equation 4). Subsequently, 16 periods between 10^{-2} s and 10^{2} s were selected for inversion, as these are the frequencies sensitive to structure beneath 250 m. In an effort to add further constraints to this inversion, the regolith and basement structures were used as a starting model with values of 10 Ωm and 1000 Ωm respectively. An initial inversion was run with a $\boldsymbol{\tau}$ of 10, and smoothing of 0.2 in x, y and z directions. However, little deviation from the starting model occurred, and an RMS of 3.38 was returned after 3 iterations.

As a feature of the WSINV3DMT algorithm, a 3D smoothing and scaling operator is applied to the distance of the current model, *m*, from the initial model, m_0 (Siripunvaraporn *et al.* 2005a). Thus, the WSINV3DMT algorithm penalises smoothed deviations from m_0, which is effectively an *a priori* constraint. In order to relax the limitation of the prior model, the inversion was re-started from the best fit model file of the previous run (iteration 3). For this inversion, a $\boldsymbol{\tau}$ of 5 with smoothing of 0.1 in x, y and z directions was utilised. After 3 iterations, an RMS of 2.09 was returned. Apart from a decreased RMS, the second run demonstrated only slightly lower resistivity values below and surrounding the survey area. Despite the improvement in model fit, the subsurface conductor was not resolved (Figure 7c).

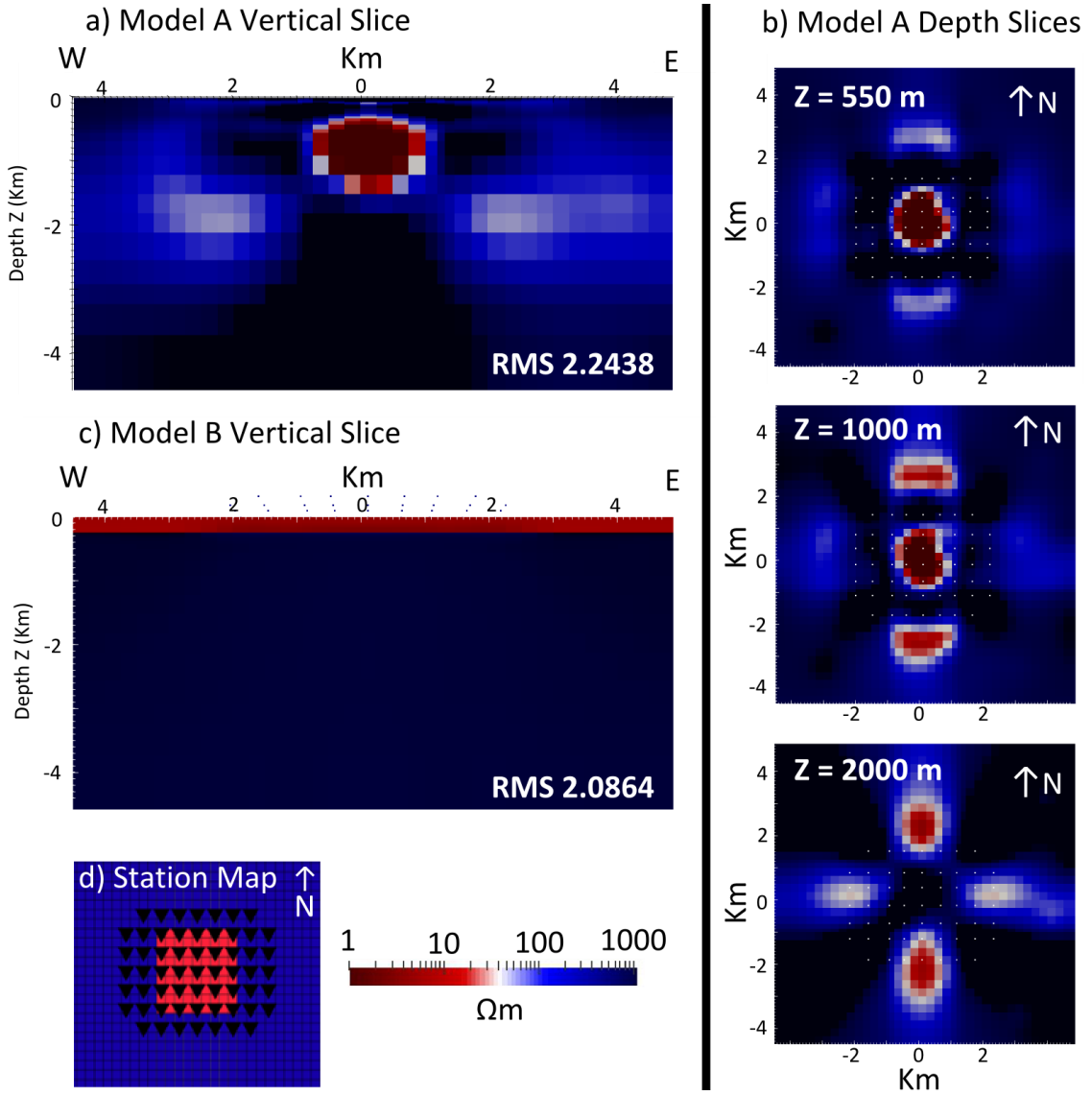

Figure 7: Results of 3D WSINV3DMT inversions of Model A and B data sets. 7a) Y-slice through the centre of Model A after 3 iterations. 7b) Depth slices of Model A at 550 m, 1000 m, and 2000 m. 7c) Y-slice through the centre of Model B after 6 iterations and 2 runs. 7d) Station map demonstrating the model station grid and lateral extent of target anomaly.

3D Inversion of a 2D Profile Line

Due to the cost and time associated with 3D surveys, most MT data are still acquired along 2D profiles. When completing 2D inversions, it is essential to first determine the geoelectric strike direction. If necessary, impedance information is mathematically rotated to this orientation so that the off diagonal components (TE and TM apparent

resistivity and phase) can be fitted with 2D inversion. By disregarding all diagonal components of the impedance tensor, an assumption must be made that the data are purely 2D. However, if 2D profile data are inverted with 3D inversion codes, and for all impedance components, no potentially erroneous dimensionality assumptions are required. To evaluate the importance of acquiring and inverting 3D survey data, the WSINV3DMT algorithm was applied to a 2D station profile of **Model A.** This profile was not positioned above the centre of the target anomaly, but towards its southern edge (Figure 8c), where the data demonstrates higher skew values and 3D effects.

Forward calculations were made for 21 station sites that were used to create inputs for the WSINV3DMT algorithm. For this inversion, the same model domain and parameters were utilised as for the 3D grid. After 4 iterations, the RMS reduced from 13.58 to 1.62.

Figure 8 shows a 2D slice across the profile and target anomaly, as well as three depth slices at 550 m, 1000 m, and 2000 m. A 1 Ωm to 10 Ωm anomalous structure is resolved north of the 2D profile. Although the target's southern edge and depth extent is not resolved, the inversion recovers the conductivity and position of the block successfully. Although inversions were completed for **Model B**, the target structure was not resolved.

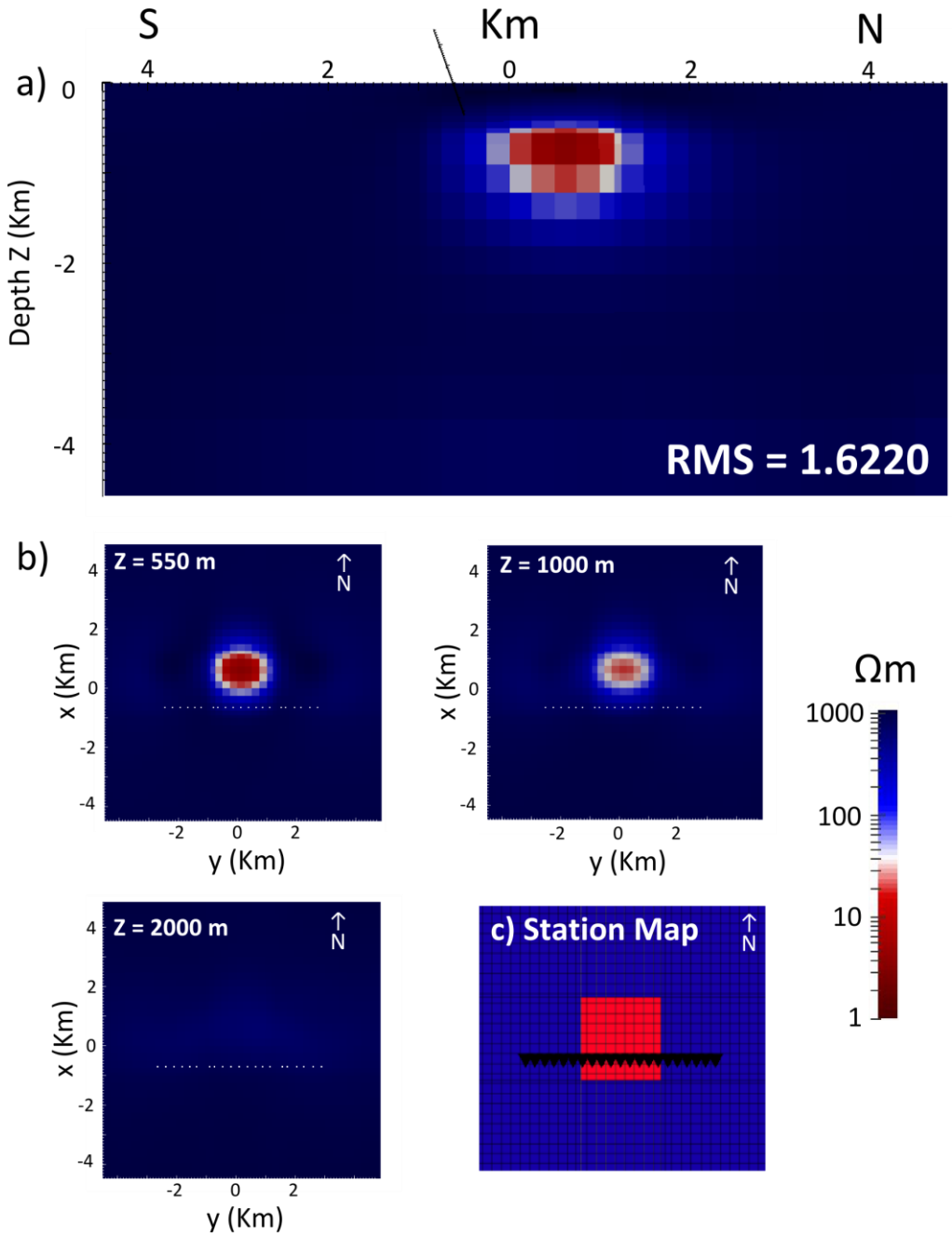

Figure 8: Model A 3D inversion result for a 2D station profile above the southern edge of the target anomaly. 8a) Vertical cross section through the centre of the target anomaly orientated S to N. 8b) Horizontal cross sections at depths of 550 m, 1000 m, and 2000 m. 8c) Station map showing the position of the target anomaly and survey profile.

3D MT SURVEY FROM THE WIRRDA WELL IOCG DEPOSIT

In the second component of this thesis, the methods of the synthetic model study have been applied to a real 3D MT data set from the Wirrda Well iron oxide copper gold (IOCG) deposit. Phase tensors are presented for all station sites and for three periods; 0.1 s, 1 s, and 10 s. In addition, 2D and 3D inversion algorithms have been applied to this data set to determine if the structural geometries of known mineralised and altered zones can be recovered with MT.

Background

The Wirrda Well IOCG mineralisation system is located on the Stuart Shelf in South Australia, approximately 25 km south-south east of Olympic Dam (Figure 9). Wirrda Well is just one of a suite of known IOCG systems of the Gawler Craton (Funk 2013), and considered an analogue of the Olympic Dam-style mineralisation (Vella 1997). The host rocks at Wirrda Well are predominantly altered granitic breccias, with mineralisation associated with hematite and magnetite veins, as well as chlorite alteration (Vella 1997). Petrophysical analysis of core samples show that mineralised and altered host rocks are more conductive than un-mineralised country rock (Vella 1997). However, this deposit exists under thick sedimentary cover sequences, which based on drilling, are interpreted to range from ~ 350 m to ~ 600 m in thickness (Vella 1997). Subsequently, MT may be rendered insensitive to structures associated with altered and mineralised rocks below these depths, as predicted by synthetic model studies.

The MT data set considered here was acquired and processed in 2009 by the University of Adelaide (SA, South Australia). This survey consists of 46 broadband MT stations (Table 2) with responses between 0.01 s and 20 seconds. The survey design consists of a 500 m spaced grid, with two station profiles orientated N45˚W and S45˚W (Figure 9).

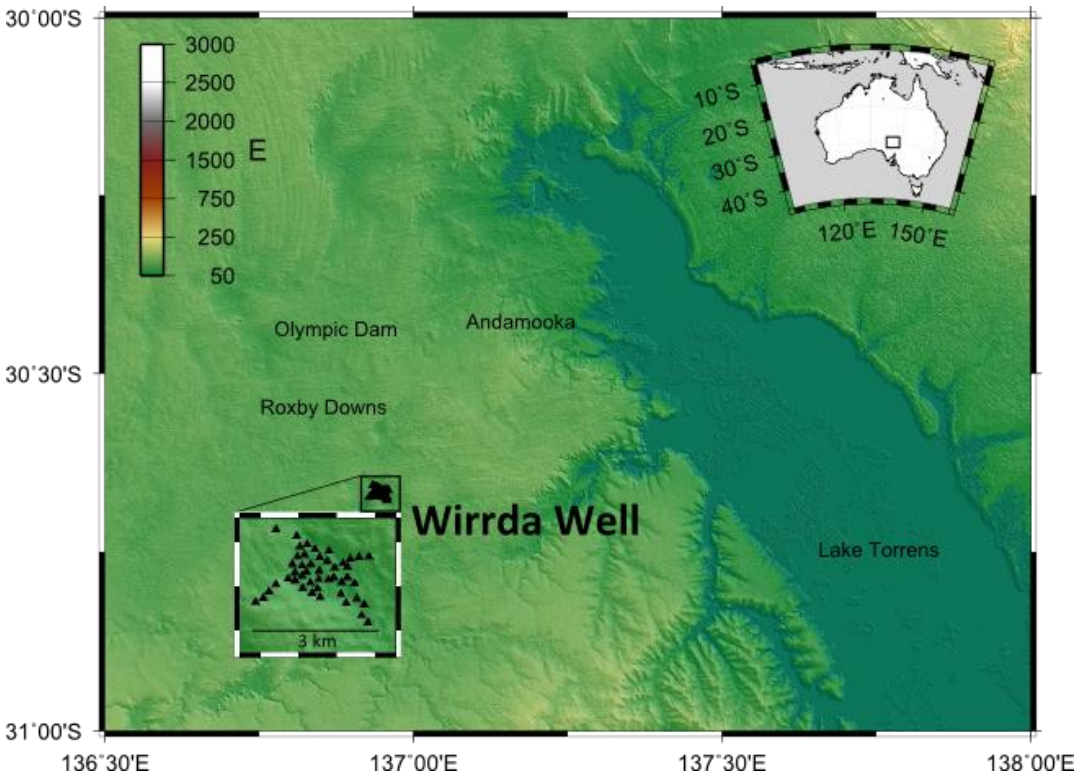

Figure 9: Regional topographic map of the Stuart Shelf indicating the location of the Wirrda Well 3D MT survey. MT station locations are marked by black triangles.

Wirrda Well Station Site Information Table

Site Name	Longitude (˚ ' ")	Latitude (˚ '")	Elevation (m)	2D Inversion	3D Inversion
WW01	136˚56'02.8320"	-30˚39'25.6322"	88	✓	
WW02	136˚56'22.2000"	-30˚39'30.8882"	81	✓	
WW03	136˚56'25.1880"	-30˚39'39.4922"	74	✓	✓
WW04	136˚56'32.2800"	-30˚39'37.6922"	73	✓	✓
WW05	136˚56'23.2800"	-30˚39'47.8082"	74	✓	✓

WW06	136°56'29.6520"	-30°39'46.4402"	73	✓	✓
WW07	136°56'39.3720"	-30°39'41.6882"	71	✓	✓
WW08	136°56'18.3480"	-30°39'54.1082"	69	✓	✓
WW09	136°55'43.7520"	-30°40'24.9602"	86		
WW10	136°55'51.0600"	-30°40'21.7922"	89		
WW11	136°55'55.9200"	-30°40'16.2122"	94		
WW12	136°56'02.7600"	-30°40'10.5602"	84		
WW13	136°56'14.4600"	-30°40'05.9522"	71		✓
WW14	136°56'20.6520"	-30°40'00.8402"	80		✓
WW15	136°56'27.1680"	-30°39'55.1882"	73	✓	✓
WW16	136°56'20.8680"	-30°40'07.3922"	69		✓
WW17	136°56'27.3480"	-30°40'03.4682"	71		✓
WW18	136°56'31.5600"	-30°40'00.1922"	74	✓	✓
WW19	136°56'35.7720"	-30°39'53.8202"	71	✓	✓
WW20	136°56'43.9800"	-30°39'48.3482"	71	✓	✓
WW21	136°56'52.9080"	-30°39'43.2722"	72		✓
WW22	136°56'27.7080"	-30°40'13.3682"	72		✓
WW23	136°56'35.1600"	-30°40'09.1922"	70	✓	✓
WW24	136°56'43.5120"	-30°39'59.4722"	70	✓	✓
WW25	136°56'51.1080"	-30°39'51.3722"	71		✓
WW26	136°56'43.0800"	-30°40'06.6002"	63	✓	✓
WW27	136°56'58.2720"	-30°39'56.7722"	75	✓	✓
WW28	136°57'05.9400"	-30°39'53.2802"	72		✓
WW29	136°57'12.4920"	-30°39'49.5722"	74		
WW30	136°57'20.9880"	-30°39'48.3122"	80		
WW31	136°57'30.7080"	-30°39'47.9882"	84		
WW32	136°56'36.4200"	-30°40'17.5802"	75		✓
WW33	136°56'42.1080"	-30°40'13.7282"	70	✓	✓
WW34	136°56'52.4400"	-30°40'06.7082"	75	✓	✓

WW35	136°56'57.5880"	-30°40'04.6202"	70	✓	✓
WW36	136°57'10.0080"	-30°39'56.2682"	66		✓
WW37	136°56'44.4120"	-30°40'21.0002"	72		✓
WW38	136°57'04.9680"	-30°40'08.5802"	74	✓	✓
WW39	136°57'10.4400"	-30°40'04.6922"	69	✓	✓
WW40	136°57'03.9600"	-30°40'18.4802"	68	✓	✓
WW41	136°57'17.1000"	-30°40'09.5522"	75		✓
WW42	136°57'09.0000"	-30°40'25.6082"	74	✓	
WW43	136°57'19.2600"	-30°40'21.9722"	74	✓	
WW44	136°57'26.1000"	-30°40'26.6522"	78	✓	
WW45	136°57'23.5080"	-30°40'35.8682"	69	✓	
WW46	136°57'29.4480"	-30°40'41.4122"	79	✓	

Table 2: 46 Magnetotelluric stations deployed at the Wirrda Well IOCG deposit. This table shows the name, location and the elevation (meters) of all survey sites. The stations utilised in 2D and 3D inversions are shown in columns 5 and 6.

Phase Tensors

Figure 10 shows map view phase tensor plots at 0.1 s, 1 s and 10 s. Phase tensors are presented with colour fills corresponding to both minimum phase (ϕ_{min}) (Figure 10a) and skew angle (β_0) (Figure 10b). At 0.1 s, tensors are approximately circular and demonstrate skew values near 0˚. This indicates 1D structure at shallow depth, which is consistent with the presence of sedimentary cover sequences. At 1 s, phase values decrease 20˚, and tensors become elongated in either NW or NE orientations. Together with skews (β_0) > 0˚, this indicates a transition from 1D cover into multidimensional and resistive basement. A 20˚ increase in phase from the SE to NW of the survey area is observed for periodicities between 0.1 and 1 s. This is likely an indication that there is an increase in the thickness of sedimentary cover towards the NW. At 10 s, tensors

become increasingly elliptical, and demonstrate high skew ($|\beta_0| \geq 5$). At > 1 s, there is a preferred orientation of ϕ_{max} for majority of sites. This indicates the presence of a regional geoelectric strike aligned ~ N45˚W.

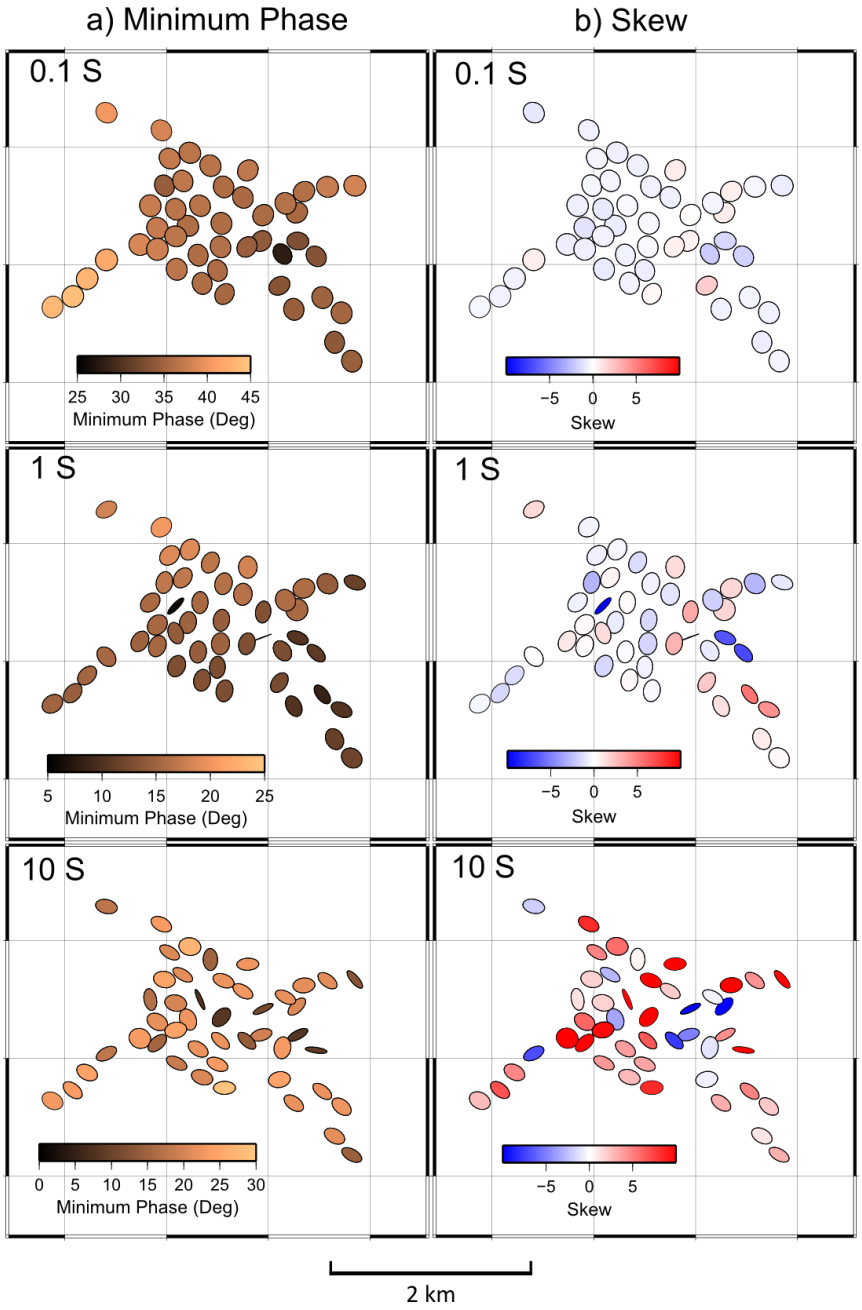

Figure 10: Map view of Wirrda Well phase tensors for three periods; 0.1 s, 1 s and 10 s. 10a) Phase tensor plots with colour fills corresponding to minimum phase (ϕ_{min}). 10b) Phase tensors plots with colour fills corresponding to skew angle. $|\beta_0| \geq 5$ indicate 3D structure (Blue and Red).

2D MT Inversion

Two-dimensional inversions were completed utilising the RLM2DI code of Rodi and Mackie (2001). 28 stations identified in Table 2 were inverted for a 2D profile orientated NW across the survey area (Figure 11). Both TE and TM modes were inverted for periods between 0.01 s and 20 s. Apparent resistivity and phase errors were set to 10% and 5% respectively, and data was rotated 45˚to geoelectric strike. The strike orientation was approximated utilising phase tensor plots shown in Figure 10. Apparent resistivity and phase plots were used to check data quality. Points that fell largely outside of the smooth curves required by the data were considered noise, and masked prior to inversion.

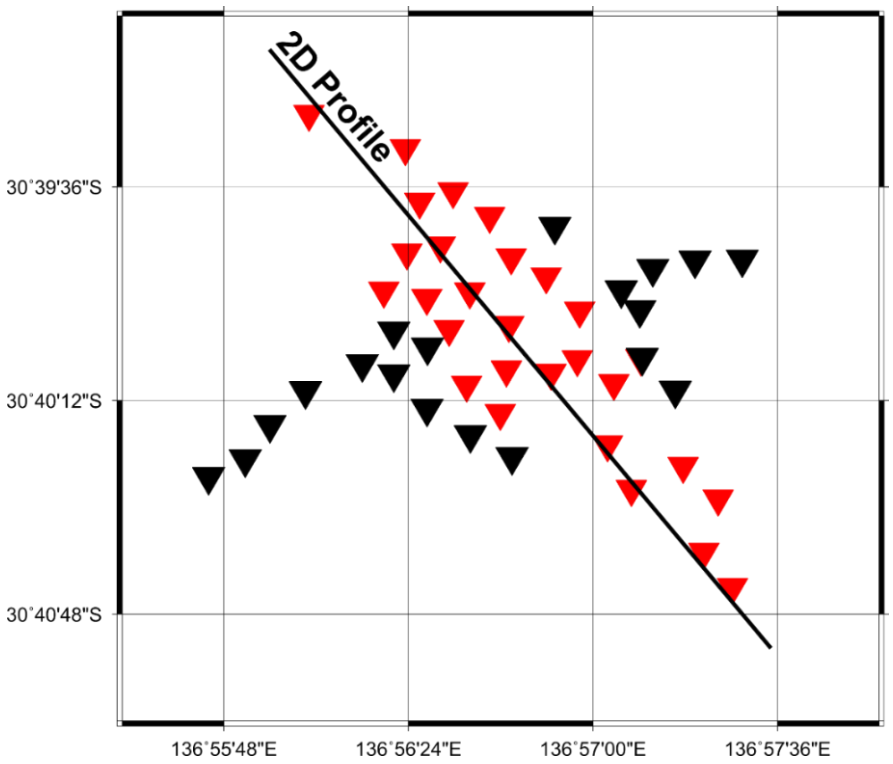

Figure 11: Wirrda well 2D profile station map. MT stations are represented by black and red triangles. Red triangles indicate active stations utilised for 2D inversions.

Figure 12 shows inversion results computed from two uniform starting models ($\boldsymbol{m_0}$) of 10 Ωm and 1000 Ωm. A $\boldsymbol{\tau}$ of 10 was determined to provide best model results, and RMS misfits of 1.77 (m_0: 10 Ωm) and 1.758 (m_0: 1000 Ωm) were returned.

A thick overlying conductive (1 - 20 Ωm) layer is resolved in both inversions shown in Figure 12. While the depth extent of this layer is typically around 400 m to 600 m, there is a high degree of heterogeneity. This structure is associated with thick and conductive cover sequences. Subsequently, the sharp conductivity contrast below this layer is interpreted as the cover/basement contact. The overlying conductive layer is shown to thicken towards the north of the profile area, where it is resolved down to 1100 meters.

When the initial model domain is 10 Ωm (Figure 12a), a less resistive zone (150 Ωm to 400 Ωm) is resolved at the centre of the model down to depths of ~ 4 km (Figure 12a). However, this structure is not observed for inversions utilising resistive starting models (1000 Ωm) (Figure 12 b).

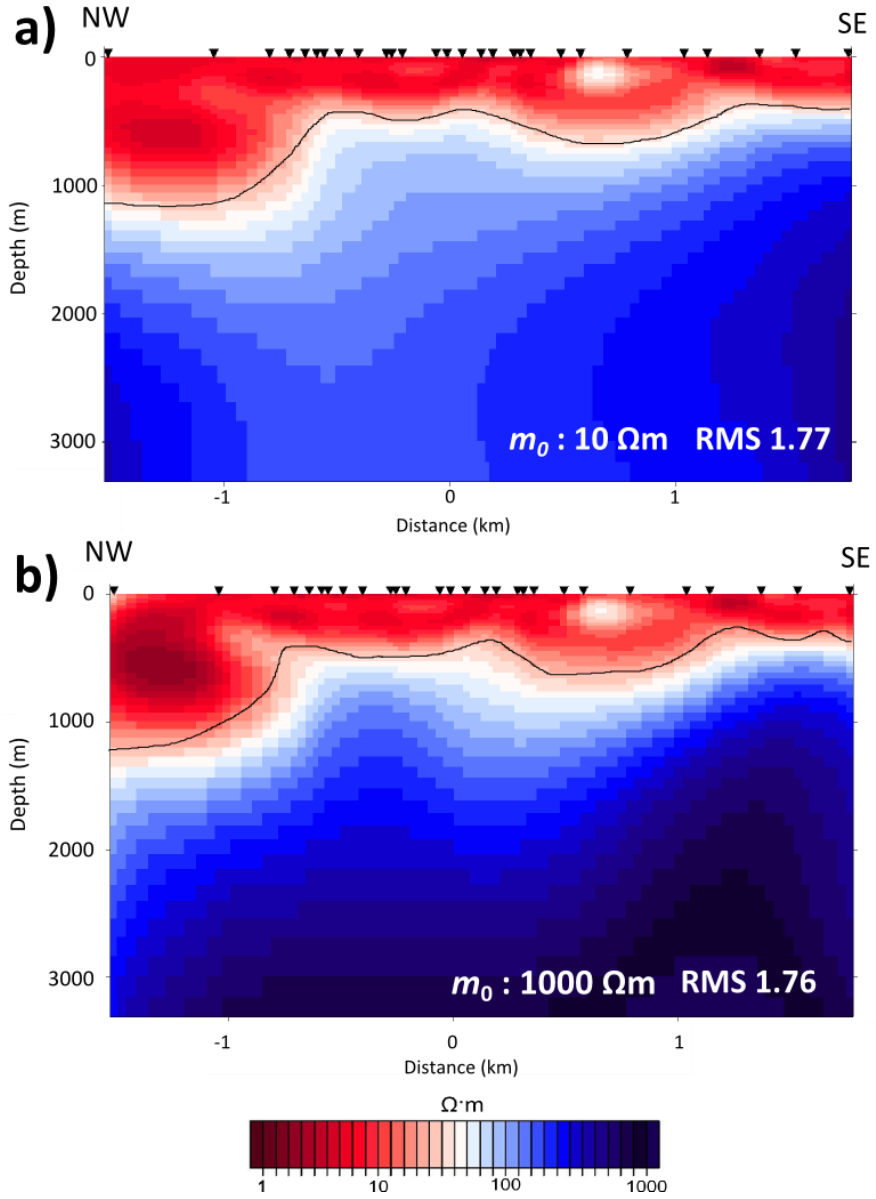

Figure 12: 2D inversion results of Wirrda Well station data for a northwest to southwest profile of 28 sites (Figure 11). 12a) m_0 = 10 Ωm. 12b) m_0 = 1000 Ωm.

3D MT Inversion

The 3D inversion algorithm WSINV3DMT (Siripunvaraporn *et al.* 2005a) was applied to the Wirrda Well data set to produce two 3D models. Due to computational limitations, only 32 sites (Table 2, Figure 13) and 16 periods between 10^{-2} s and 20 s could be inverted for all complex impedance terms. In addition, elevation and topography information could not be included in computations. The model domain

consisted of a 100 km rectilinear cube, discretised by $N_x \bullet N_y \bullet Nz = 68 \bullet 59 \bullet 40 = 160480$ cells. Two inversions were executed with a 5 % error in impedance information, but with different initial models ($\boldsymbol{m_0}^x$). Whilst the first computation was executed from a 100 Ωm half-space ($\boldsymbol{m_0}^1$), a second starting model ($\boldsymbol{m_0}^2$) incorporated 400 m of 10 Ωm cover and a 1000 Ωm basement. For $\boldsymbol{m_0}^2$, both the depth to basement and resistivity of each component were approximated from 2D inversion results shown in Figure 12b. Each model was initially run with a $\boldsymbol{\tau}$ of 5, and smoothing of 0.3 in x, y and z directions. After 3 iterations both models were stopped, and the best fit model file (iteration 3) was used as the starting condition for a second run utilizing a $\boldsymbol{\tau}$ of 5 and smoothing of 0.1. The results of each inversion are presented in Figure 14. Despite similar RMS misfits ($\boldsymbol{m_0}^{1:}$ 1.7, $\boldsymbol{m_0}^2$: 1.49), the results from each inversion are strikingly different.

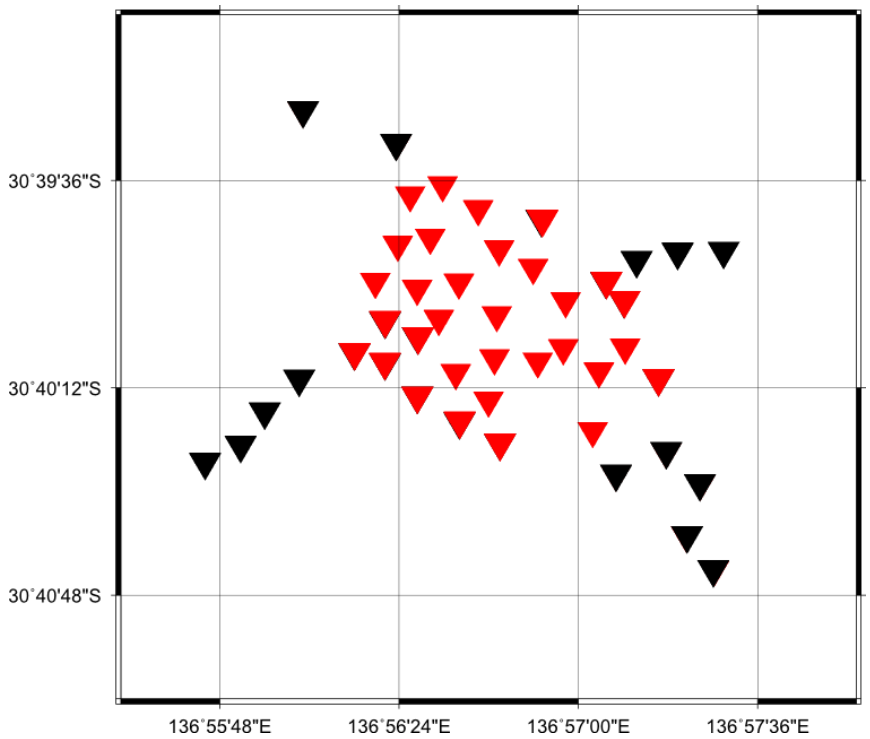

Figure 13: Station location map of 3D inversion sites. MT stations are shown as black and red triangles. Red triangles indicate active sites utilised in 3D inversions.

For $\boldsymbol{m_0}^1$, an RMS error of 1.7 was returned after 7 iterations (Figure 14a). The top 500 m of this model result is comprised of a conductive (1 - 20 Ωm) cover sequence. However, the thickness of this layer is highly heterogeneous, and increases to ~ 800 m towards the north, south, and east of the survey area. In addition, a number of resistive bodies (~ 100 – 1000 Ωm) are resolved within its structure. At depths > 500 m, most of the survey area shows apparent resistivity values between 200 Ωm and 1000 Ωm. However, a number of conductive (1 – 10 Ωm) vertical pipes are also resolved. These anomalous conductors have diameters of ~ 500 m, and extend downwards ≥ 5000 m. However, at depths ≥ 1000 m, these anomalies are mostly located either outside, or at the edge of the survey area.

For $\boldsymbol{m_0}^2$, an RMS error of 1.49 was returned after 6 iterations (Figure 14b). In this model, the overlying conductive (1 – 10 Ωm) layer terminates at 400 m. At this depth, there is a sharp change in resistivity attributed to the constraints placed on the inversion from the prior model ($\boldsymbol{m_0}^2$). Although its resistivity is higher below 400m (100 – 700 Ωm), structure associated with the overlying cover is observed down to 800 m. The resistivity values within the basement are typically much higher (≥ 1000 Ωm) for this inversion. In addition, there is little structure resolved at the edges of the survey and at depths greater than 1000 m.

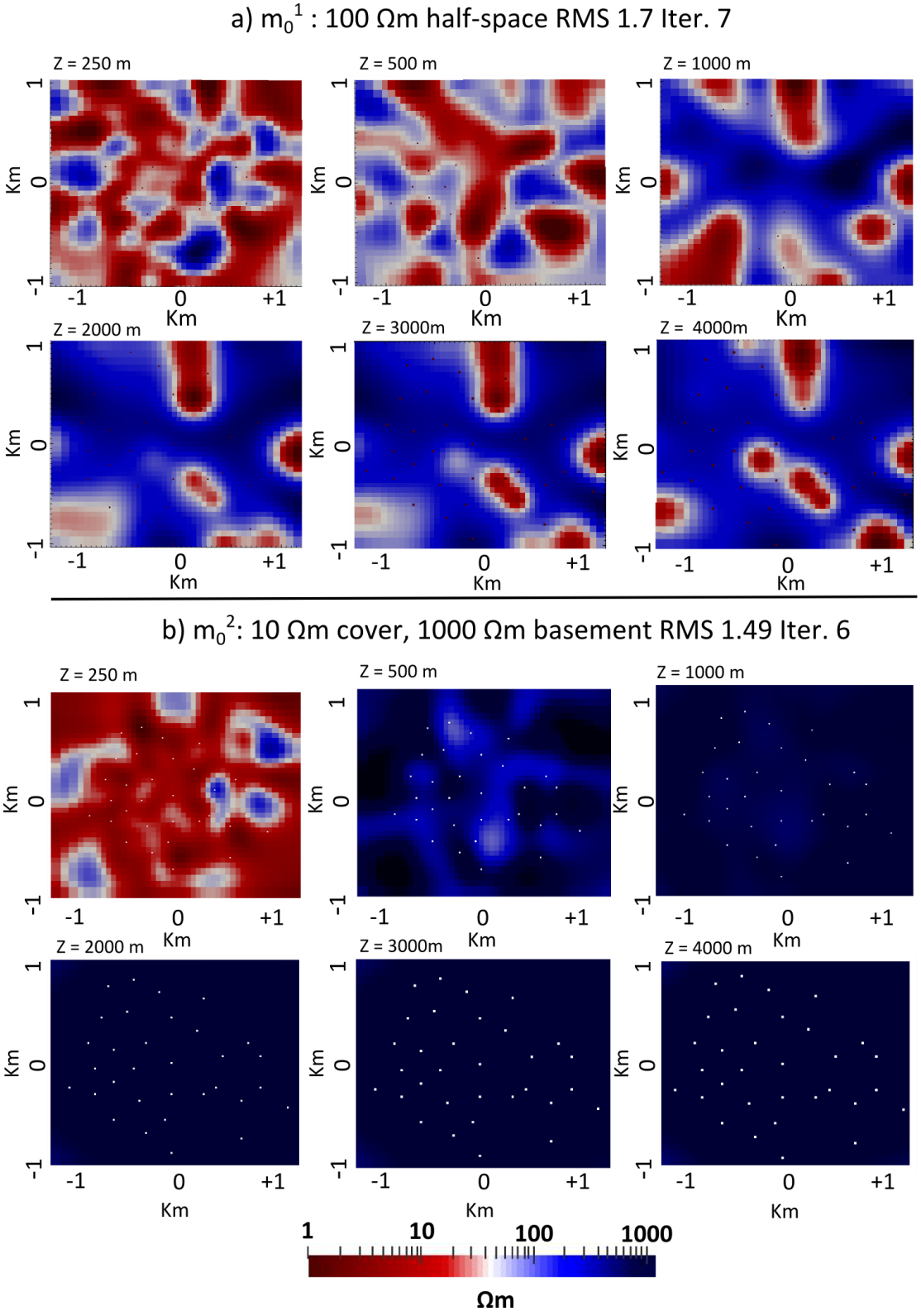

Figure 14: 3D inversion results of the Wirrda Well survey utilising two starting models (m_0). 14a) m_0: 100 Ωm half-space. Depth slices at 250 m, 500 m, 1000 m, 2000 m, 3000 m and 4000 m after 7 iterations. 14b) m_0: 400 m of 10Ωm cover and 1000Ωm basement. Depth slices at 250 m, 500 m, 1000 m, 2000 m, 3000 m and 4000 m after 6 iterations.

DISCUSSION

Synthetic Model Study

Synthetic 3D forward modelling and inversion was an effective way of demonstrating the possible limitations of MT in delineating subsurface 3D conductivity structure. Comparisons between the synthetic data sets of **Model A** and **B** highlight the danger associated with electromagnetic exploration in areas with thick conductive cover. For **Model B** with cover, there was an almost complete inability to detect the 3D target. Although 2D and 3D inversions successfully returned depth to basement information, the target structure was not resolved. Conversely, inversions for an extended 2D body returned the model structure successfully, attributed to a significant difference between the TE mode responses of each scenario. This suggests that to detect and image 3D conductive structures under conductive cover, they must be very large relative to its thickness, or alternatively, show an elongation along one orientation. However, if the length of the target is not sufficient, 2D inversions of profiles above this target will recover incorrect conductivity structures resulting from distortion caused by the current channelling effect (see Jones 1983, Wannamaker *et al.* 1984, Berdichevsky *et al.* 1998).

For **Model A**, the sensitivity of MT to the target anomaly is greatly increased at shorter sounding periodicities. As there is a large response in the data, phase tensor and induction arrows show a strong induction polarisation associated with a large and conductive subsurface body. Additionally, both 2D and 3D inversions gave model results that agreed with the true model conductivity structure. However, only half of the targets depth extent could be resolved. It may be possible that additional long period data may help to resolve the target body at depth. This is particularly true for 3D

inversions of **Model A**, where the longest period data is 10 s, corresponding to a penetration of 1600 m within a 1 Ωm host (Equation 4). However, it is well known that it is difficult to resolve the bottom of conductive structure with MT (Newman & Alumbaugh 2000, Siripunvaraporn & Egbert 2000, Siripunvaraporn *et al.* 2005a), which is an intrinsic property of induction data.

Although 3D inversions are preferred, successful identification of the target anomaly was achieved using 2D inversion. Additionally, 3D inversions of a 2D profile gave similar results to inverting for a 3D grid. The target anomaly was resolved with high resolution away from the station profile. This recovery of nearby 3D resistivity structure is comparable with results of Siripunvaraporn *et al.* (2005b) and Lin *et al.* (2011). Although 3D surveying is relatively expensive and time-consuming, for many cases it may be possible to make successful interpretations utilising 3D inversions of 2D profile data alone. However, this work suggests that it is warranted to test the applicability of this approach with more complex synthetic model structures.

Tipper data successfully indicated the presence of conductive targets at depth (through Parkinson induction arrows), but it remains unclear if similar results would be achieved with real data, and in the presence of strong regional induction polarisations (i.e. near basins, ranges).

3D MT Survey from the Wirrda Well IOCG

2D and 3D inversion codes were applied to the Wirrda Well data set in an attempt to recover anomalous conductivity structure associated with altered and mineralised

basement rock. In all model results, a conductive (1 – 10 Ωm) cover is resolved above a resistive basement. This can also be observed in the data, where phase tensors (Figure 10) indicate a decrease in minimum phase with depth, as well as a transition from 1D to multidimensional geoelectric structure. The thickness of this cover is typically resolved between 400 m and 800 m, which is consistent with depth interpretations made from drill hole data (Vella 1997). Below these depths, both 2D and 3D inversion results are not independent of the starting models ($\boldsymbol{m_0}$) utilised.

When 2D inversions are computed from low resistivity starting models (10 Ωm), there is a preference of the inversion to resolve anomalous (100 - 400 Ωm) structure within the basal units (~ 1000 Ωm). These structures cannot be resolved when the starting model is resistive (1000 Ωm). Comparisons between each inversion demonstrates that there is little reliability in the models below the conductive cover. As there is no requirement within the data, structure resolved in the basement is likely erroneous and misleading.

For most station sites, the beta criterion (Caldwell *et al.* 2004) significantly deviates from zero at > 0.1 s (Figure 10b). Thus, this data set is influenced by the presence of 3D basement structure. As the 2D assumption may not be appropriate, 3D inversions were computed incorporating all complex impedance components. 3D model results demonstrate the risk associated with taking a naïve and simplistic approach to 3D inversion.

The WSINV3DMT algorithm searches for the smallest deviation from the prior or initial model (Siripunvaraporn *et al.* 2005a). Subsequently, the existence of an *a priori* starting condition is unavoidable. Two starting models ($\boldsymbol{m_0}^1$ $\boldsymbol{m_0}^2$) were utilised for 3D inversions of the Wirrda Well data set. Although each inversion returned a similar RMS misfit ($\boldsymbol{m_0}^{1:}$ 1.7, $\boldsymbol{m_0}^2$: 1.49), the resistivity structures below 800 m are vastly different. Comparisons between each 3D inversion (Figure 14) shows that the overall resistivity structure returned by the WSINV3DMT algorithm is greatly biased by the resistivity of the starting model ($\boldsymbol{m_0}$). Consequently, spurious and misleading structure is shown to be introduced into the model when the resistivity distribution of $\boldsymbol{m_0}$ is not geologically appropriate. In this case, model results were stabilised by utilising a two layered *a priori* model ($\boldsymbol{m_0}^2$), which was based on the background conductivity structure recovered from 2D inversions (cover and basement). This result highlights the importance of incorporating *a priori* information when the 3D model regularisation is dependent on the starting model (see also Newman *et al.* 2003, Tietze & Ritter 2013).

The sensitivity of the 2D and 3D models was tested by computing inversions from contrasting resistivity values. Comparisons between results allowed for the least and most reliable areas of each model to be determined qualitatively. In all cases, only recovery of structures associated with conductive cover sequences can be shown to be robust. The discrepancies between model results at depths > 1000 m indicates that the resolution of long period MT data (1 - 10 s) may not be trusted due to noise. In addition, synthetic model studies suggest that even if highly conductive and large 3D targets do exist beneath the thick (~ 400 – 800m) cover at Wirrda Well, there will be minimal

response in the data. This result underscores the importance of acquiring quality and reliable long period (1 – 100 s) data.

CONCLUSIONS

The proficiency of 2D and 3D MT inversion in delineating 3D structural geometry has been systematically tested with synthetic data. Comparisons between model responses demonstrate that the resolution of MT to detect finite 3D bodies is greatly reduced under conductive cover. Where no cover exits, 2D inversions can recover the first order structure of 3D bodies, and should be used in conjunction with 3D methods. Where only 2D profile data is available, successful interpretations can be made utilising 3D inversion algorithms that return nearby resistivity structure.

While 2D and 3D inversion can resolve the thickness of cover above the Wirrda Well IOCG, conductivity structure associated with basement alteration and mineralisation is not recovered. Model results demonstrate that due to the solution uncertainty inherent to 3D approaches, sensitivity analysis must be completed to avoid interpretations of erroneous and misleading structure.

From this study, it is clear that caution must be taken when commissioning explorative 3D MT surveys in regions of thick and conductive cover. In such circumstances, it is possible that the response of significant 3D targets will be masked, resulting in misleading interpretations of MT data and inversions.

ACKNOWLEDGMENTS

I would like to thank my primary supervisor Professor Graham Heinson for his guidance and feedback throughout this project. I would also like to thank Dr. Stephan Thiel, Kate Robertson, Paul Soeffky, Theo Aravanis of Rio Tinto and Bob Smith, for their suggestions and assistance throughout the year. A special thanks to Dr Lars Krieger for his advice and help in setting up the 3D inversion code, without which this project would not be possible.

REFERENCES

BERDICHEVSKY M. N., DMITRIEV V. I. & POZDNJAKOVA E. E. 1998. On two-dimensional interpretation of magnetotelluric soundings. *Geophysical Journal International* **133**, 585-606.

BIBBY H. M., CALDWELL T. G. & BROWN C. 2005. Determinable and non-determinable parameters of galvanic distortion in magnetotellurics. *Geophysical Journal International* **163**, 915-930.

BOOKER J. 2013. The Magnetotelluric Phase Tensor: A Critical Review. *Surveys in geophysics*, 1-34.

CAGNIARD L. 1953. Basic Theory of the Magnetotelluric Method of Geophysical Prospecting. *Geophysics* **18**, 605-635.

CALDWELL T. G., BIBBY H. M. & BROWN C. 2004. The magnetotelluric phase tensor. *Geophysical Journal International* **158**, 457-469.

CHEN X.-B., LÜ Q.-T. & YAN J.-Y. 2012. 3D electrical structure of porphyry copper deposit: A case study of Shaxi copper deposit. *Applied Geophysics* **9**, 270-278.

FARQUHARSON C. G. & CRAVEN J. A. 2009. Three-dimensional inversion of magnetotelluric data for mineral exploration: An example from the McArthur River uranium deposit, Saskatchewan, Canada. *Journal of Applied Geophysics* **68**, 450-458.

FERGUSON M. 2012. Searching the Deep Earth: A vision for exploration geoscience in Australia. 34th International Geological Congress, Brisbane (unpubl.).

FUNK C. 2013. Geophysical vectors to IOCG mineralisation in the Gawler Craton. *ASEG Extended Abstracts* **2013**, 1-5.

GUILBERT J. M. & LOWELL J. D. 1974. Variations in Zoning Patterns in Porphyry Ore-Deposits. *Cim Bulletin* **67**, 99-109.

HAN N., NAM M. J., KIM H. J., SONG Y. & SUH J. H. 2009. A comparison of accuracy and computation time of three-dimensional magnetotelluric modelling algorithms. *Journal of Geophysics and Engineering* **6**, 136.

JONES A. 1983. The problem of current channelling: A critical review. *Geophysical surveys* **6**, 79-122.

KEAREY P. 2002. *An introduction to geophysical exploration / Philip Kearey, Michael Brooks, Ian Hill*. Malden, MA : Blackwell Science, Malden, MA.

LEDO J. 2005. 2-D Versus 3-D Magnetotelluric Data Interpretation. *Surveys in geophysics* **26**, 511-543.

LEDO J., QUERALT P., MARTI A. & JONES A. G. 2002. Two-dimensional interpretation of three-dimensional magnetotelluric data: an example of limitations and resolution. *Geophysical Journal International* **150**, 127.

LI X., LI Y., MENG X., HAUTOT S., GOLDAK D., TARITS P. & KOSTENIUK P. 2011. Three-dimensional magnetotelluric inversion of large data sets: Case study of Pasfield Lake (Saskatchewan) for mineral exploration. *In*, *International Workshop on Gravity, Electrical & Magnetic Methods and Their Applications, Beijing, China, October 10–13, 2011*, pp 50-50.

LILLEY F. & ARORA B. 1982. The sign convention for quadrature Parkinson arrows in geomagnetic induction studies. *Reviews of Geophysics* **20**, 513-518.

LIN C.-H., TAN H.-D. & TONG T. 2011. The Possibility of Obtaining Nearby 3D Resistivity Structure from Magnetotelluric 2D Profile Data Using 3D Inversion. *Chinese Journal of Geophysics* **54**, 72-83.

LOWELL J. D. & GUILBERT J. M. 1970. Lateral and Vertical Alteration-Mineralization Zoning in Porphyry Ore Deposits. *Economic Geology* **65**, 373-&.

MACKIE R. L., SMITH J. T. & MADDEN T. R. 1994. Three-dimensional electromagnetic modeling using finite difference equations: The magnetotelluric example. *Radio Science* **29**, 923-935.

MIENSOPUST M. P., QUERALT P., JONES A. G. & MODELLERS T. D. M. 2013. Magnetotelluric 3-D inversion—a review of two successful workshops on forward and inversion code testing and comparison. *Geophysical Journal International*.

MORRISON H. F. & NICHOLS E. A. 1997. Mineral exploration with natural electromagnetic fields. *Proceedings of exploration 97: Fourth Decennial International Conference on Mineral Exploration,* Toronto, pp. 527-538.

NEWMAN G. A. & ALUMBAUGH D. L. 2000. Three-dimensional magnetotelluric inversion using non-linear conjugate gradients. *Geophysical Journal International* **140**, 410-424.

NEWMAN G. A., RECHER S., TEZKAN B. & NEUBAUER F. M. 2003. 3D inversion of a scalar radio magnetotelluric field data set. *Geophysics* **68**, 791-802.

PARKINSON W. D. 1959. Directions of Rapid Geomagnetic Fluctuations. *Geophysical Journal International* **2**, 1-14.

RODI W. & MACKIE R. L. 2001. Nonlinear conjugate gradients algorithm for 2-D magnetotelluric inversion. *Geophysics* **66**, 174-187.

SASAKI Y. 2004. Three-dimensional inversion of static-shifted magnetotelluric data. *Earth, planets and space* **56**, 239-248.

SCHODDE R. 2010. Declining Discovery rate - what is the real story? AMIRA International's 8th Exploration Managers Conference, Yarra Valley, Victoria (unpubl.).

SILLITOE R. H. 2010. Porphyry copper systems. *Economic Geology* **105**, 3-41.

SIMPSON F. & BAHR K. 2005. *Practical magnetotellurics*. Cambridge University Press.

SIRIPUNVARAPORN W. & EGBERT G. 2000. An efficient data-subspace inversion method for 2-D magnetotelluric data. *Geophysics* **65**, 791-803.

SIRIPUNVARAPORN W., EGBERT G., LENBURY Y. & UYESHIMA M. 2005a. Three-dimensional magnetotelluric inversion: data-space method. *Physics of the Earth and Planetary Interiors* **150**, 3-14.

SIRIPUNVARAPORN W., EGBERT G. & UYESHIMA M. 2005b. Interpretation of two-dimensional magnetotelluric profile data with three-dimensional inversion: synthetic examples. *Geophysical Journal International* **160**, 804-814.

TIETZE K. & RITTER O. 2013. Three-dimensional magnetotelluric inversion in practice—the electrical conductivity structure of the San Andreas Fault in Central California. *Geophysical Journal International* **195**, 130-147.

TIKHONOV A. 1950. On determining electrical characteristics of the deep layers of the earth's crust. *Sov. Math. Dokl*, pp. 295-297.

TUNCER V., UNSWORTH M. J., SIRIPUNVARAPORN W. & CRAVEN J. A. 2006. Exploration for unconformity-type uranium deposits with audiomagnetotelluric data: A case study from the McArthur River mine, Saskatchewan, Canada. *Geophysics* **71**, B201-B209.

VARENTSOV I. M., KULIKOV V. A., YAKOVLEV A. G. & YAKOVLEV D. V. 2013. Possibilities of magnetotelluric methods in geophysical exploration for ore minerals. *Izvestiya, Physics of the Solid Earth* **49**, 309-328.

VELLA L. 1997. Interpretation and modelling, based on petrophysical measurements, of the Wirrda well potential field anomaly, South Australia. *Exploration Geophysics* **28**, 299-306.

WANNAMAKER P., HOHMANN G. & WARD S. 1984. Magnetotelluric responses of three-dimensional bodies in layered earths. *Geophysics* **49**, 1517-1533.

WIGHT D. E. 1988. SEG standard for MT and EMAP data. *1988 SEG Annual Meeting*.